Progress In Electromagnetics Research, Vol. 186, 52–63, 1026

(Received 26 April 2026, Accepted 2 September 2026, Scheduled 25 September 2026)

# Giant Enhancement of Third-Harmonic Generation Enabled by Dual-Resonant Nonlocal Metagrating

Esha Maqbool, Guangdong Wang, Kaili Sun, and Zhanghua Han*

*Shandong Provincial Key Laboratory of Optics and Photonic Devices, Center of Light Manipulation and Applications*
*School of Physics and Opto-Electronics, Shandong Normal University, Jinan 250358, China*

**ABSTRACT:** Nonlinear light-matter interactions have greatly benefited from high-Q resonances, which enhance the local field at the pump frequency, strengthening the nonlinear polarization at the harmonic frequency. However, despite the strong harmonic buildup, the collected signal often remains limited by the absence of efficient radiative channels. To address this issue, we propose an all-dielectric nonlocal ternary metagrating that combines a high-Q quasi-guided-mode resonance at the fundamental frequency ($\omega$) with a moderate-Q radiative guided-mode resonance at the third-harmonic frequency ($3\omega$), leading to significantly enhancing the third-harmonic generation (THG) process. By reducing the Brillouin zone to one-third of its original size, the ternary design folds the dispersive guided-mode branches to the $\Gamma$-point, enriching the modal landscape. In addition, the ternary geometry reduces coupling into unwanted higher-order diffraction channels near $3\omega$, thereby favoring the desired harmonic radiative response. Experimentally, the device achieves an estimated collected THG conversion efficiency of approximately $1.86\times10^{-6}$, confirming the practical potential of the dual-resonant scheme. These findings establish a practical route toward dual-resonant enhancement that reduces reliance on extremely high-Q or flat-band resonances, offering a more fabrication-friendly, experimentally accessible platform for nonlinear photonic applications such as Raman spectroscopy, nonlinear imaging, and quantum photonics.

## 1. INTRODUCTION

Nonlinear optical materials have become indispensable in modern photonics due to their unique ability to generate electromagnetic radiation at frequencies absent from the incident field, underpinning applications in light sources, nonlinear imaging, optical communications, and quantum light generation [1–7]. However, the weak nonlinear response of natural bulk materials demands extended propagation lengths, while phase-matching conditions impose added fabrication complexity, necessitating compact, efficient subwavelength devices [8–11]. Among them, metasurfaces, through the resonant engineered behavior of optically thin arrays of subwavelength meta-atoms, offer a powerful route to enhance and control nonlinear optical processes by manipulating phase, amplitude, and polarization of light, while also relaxing the stringent phase-matching requirements of bulk media [10–15]. Over the past decade, both plasmonic and dielectric metasurfaces have been widely explored for nonlinear frequency conversion processes such as second- and third-harmonic generation (SHG and THG) [13–18]. Nonlinear plasmonic metasurfaces were among the earliest considerations employing localized surface plasmon resonances, which strongly concentrate electromagnetic fields at the nanoscale. Although recent experimental studies have shown that plasmonic and hybrid metasurfaces can achieve high-Q resonances despite metallic losses [19, 20], Ohmic dissipation, nonradiative loss, and thermal effects in metallic components remain important practical considerations, particularly under high-intensity nonlinear optical excitation [1, 14, 21]. In contrast, all-dielectric metasurfaces provide a complementary low-loss platform with intrinsically lower absorption losses, generally higher damage tolerance, strong volumetric field confinement, and mature fabrication compatibility. Moreover, their optically induced Mie-type multipolar resonances effectively enhance nonlinear optical processes while avoiding severe Ohmic losses [8, 12, 14, 22, 23]. Despite these advantages, conventional Mie resonances have low quality factors (Q-factors) due to radiation leakage. This directly limits photon lifetime and thus light-matter interaction strength, necessitating the development of high-Q resonances in all-dielectric nanostructures for nonlinear nanophotonics [6, 8, 15, 22].

Most high-Q strategies rely on extended collective (nonlocal) behavior rather than on localized resonances confined to individual meta-atoms, as they enable coherent field buildup and suppress radiative leakage. These high-Q resonances often originate from bound modes, that is, bound states in the continuum (BICs) and guided modes (GMs). A BIC embedded within the radiation continuum remains decoupled from external radiation by symmetry or destructive interference. A slight symmetry breaking can yield a quasi-BIC (QBIC) with an ultra-high finite Q, Fano resonance, and strong field confinement. However, their rapidly deteriorating Q-factors away from the BIC condition limit their performance under focused excitation [13, 24–26]. In contrast, GMs are intrinsically confined below the light cone and cannot couple to free-space radiation because of momentum mismatch. When periodic perturbations supply the missing momentum and fold the GM dispersion into the radiation continuum, these modes become quasi-

* Corresponding author: Zhanghua Han (zhan@sdnu.edu.cn).

guided modes (QGMs), a special type of guided-mode resonance (GMR), that retain the high-Q characteristics of the parent GMs while acquiring radiative accessibility. Compared with QBICs, QGMs have a broader dispersion, rendering their Q-factors less sensitive to variations in wavevector and frequency, while enabling greater spectral tunability and preserving high-Q characteristics [12, 22, 26–30].

Since the intensity of harmonic generation ($P(3\omega) = \varepsilon_0 \chi^{(3)} [E(\omega)]^3$) is largely determined by the field enhancement at the fundamental frequency (FF, $\omega$), tailoring a high-Q resonance to coincide with the pump excitation can significantly enhance the generated nonlinear signal at third-harmonic frequency (THF, $3\omega$) [8, 31, 32]. Nevertheless, THG is a two-frequency nonlinear phenomenon, and enhanced signal generation alone does not guarantee efficient far-field emission. In many cases, the generated harmonic light remains confined within the structure, resulting in poor extraction and limited collected output, while excessive field buildup at the FF can also accelerate the onset of saturation [8, 33]. Introducing a second resonance at THF can provide an efficient outcoupling channel for induced nonlinear polarization, enabling the generated signal to be emitted into the far field. Such a dual-resonance scheme is therefore very important, as it synergistically enhances nonlinear generation and enables efficient signal extraction, allowing performance improvement by orders of magnitude over conventional single-resonance designs. However, realizing such structures often requires meticulous engineering of the size, shape, and orientation of the constituent elements, making them difficult to fabricate and highly sensitive to structural imperfections and parametric deviations [9, 10, 21, 33–38]. Although prior studies have explored dual-resonant harmonic generation in metasurfaces, especially including demonstrations in graphene-based platforms [21, 33–39], to the best of our knowledge, experimental demonstrations of all-dielectric period-tripled (ternary) metagratings that combine a folded pump-side resonance with a harmonic-side GMR for enhanced THG remain limited (a representative comparison is provided in Table S3 of the Supporting Information).

To address this challenge, we propose a fabrication-tolerant ternary metagrating on a slab platform that supports dual-resonant operation by combining a high-Q resonance at the FF with a well-defined radiative resonance at the THF. The key innovation lies in exploiting period tripling to reduce the Brillouin zone, which offers steeper dispersion, a smaller spectral gap, and a richer Γ-accessible modal landscape. This enables robust $\omega$–$3\omega$ spectral matching through simple slab thickness modulation, simultaneously providing efficient field buildup at the FF and efficient outcoupling at the THF. Compared with binary counterparts, our ternary design offers at least an order of magnitude higher THG conversion efficiency, lower diffraction leakage, and superior tunability. Experimentally, we achieved an estimated collected THG conversion efficiency of approximately $1.86 \times 10^{-6}$, demonstrating practical performance comparable to or higher than that of previously reported flat-band [6] and ultrahigh-Q single-resonant [12] structures under closely related excitation and collection conditions, offering practical and fabrication-tolerant pathways for a wide range of nonlinear applications.

## 2. RESULTS

Fig. 1 shows a comparison of the proposed dual-resonant ternary design and a conventional single-resonant metagrating, highlighting the necessity for both strong near-field enhancement at the FF and efficient far-field outcoupling at the THF. In conventional single-resonant structures, the resonance is typically engineered only at the FF to strengthen the nonlinear polarization buildup responsible for THG, as illustrated in Fig. 1(a). However, without an efficient radiative channel at the harmonic frequency, the generated signal cannot be effectively extracted into the far field and is instead partially lost in unwanted channels, resulting in weak collected THG. In contrast, the proposed dual-resonant design supports resonances at both the FF and THF, thereby preserving strong THG while enabling far-field radiation of the generated signal [1, 34–36], as illustrated in Fig. 1(b). Under similar-Q resonance conditions, the nonlinear polarizations at THF for both single-resonant and dual-resonant structures would be similar. However, the enhanced far-field outcoupling efficiency, due to the radiative channel, would result in higher collected THG in the dual-resonant structure. Figs. 1(c) and (d) show the physical origin of this improved THG extraction. In the ternary structure, the smaller parent-lattice spacing associated with the three-element unit cell reduces coupling of the THF mode into allowed higher-order diffraction orders, thereby favoring the desired radiative response. Consequently, the ternary dual-resonant design provides a more efficient outcoupling pathway for the generated harmonic signal and is therefore expected to produce substantially stronger THG under similar excitation conditions.

The advantage of the ternary design can be better understood in terms of the Brillouin zone folding (BZF) order ($m$, an integer). A powerful route for making guided modes (GMs) accessible to free-space radiation is to tailor BZF through controlled perturbations of the parent unit cell [29, 40, 41]. Importantly, the unit-cell perturbation determines both the enlarged period and the folding order. Increasing the folding order introduces additional folded branches, expands the accessible dispersion landscape, and preserves a small adjacent grating spacing, which may provide greater freedom to position resonances at the desired wavelengths under normal incidence. As a result, higher-order zone folding offers an attractive route for modal landscape engineering by expanding the set of resonant candidates available for $\omega$–$3\omega$ spectral alignment.

Fig. 2 summarizes this concept, and schematically shows how the dispersion bands of an underlying unary grating are mapped into the reduced first Brillouin zone (FBZ) under the $m$-th order ($m = 1, 2, 3$) folding. When the original unit cell with period $P$ is modified to $P_m = mP$ by perturbing every $m$-th element, the FBZ is reduced from $[-\pi/P, \pi/P]$ to $[-\pi/mP, \pi/mP]$, allowing additional modes to be folded into accessible momentum space and thereby increasing the overall design flexibility. As $m$ increases, the FBZ width decreases, and additional bands are folded into the reduced zone, enriching the modal landscape accessible under normal incidence. This folding process can relocate band-edge features, gaps, and steeper dispersion segments to new positions within

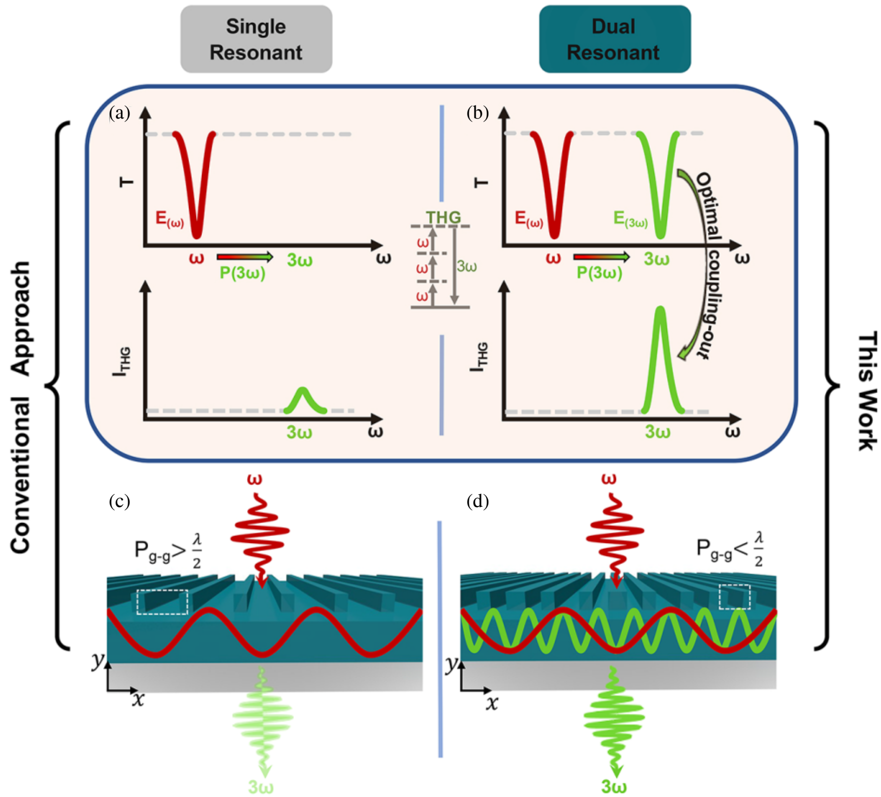


**FIGURE 1**. Comparative illustration of spectral characteristics and THG efficiency between single-resonant and dual-resonant metagrating approaches. (a) A single-resonant structure, resonating at the FF ($\omega$), preserving efficient nonlinear polarization buildup but weak collected THG due to the lack of a well-defined radiative channel at the THF ($3\omega$). (b) In contrast, a dual-resonant structure, which supports well-defined resonances at both the pump and THF, preserves efficient nonlinear polarization buildup while enabling efficient radiative outcoupling, leading to significantly enhanced THG radiation. The inset in the middle illustrates the energy level transitions associated with THG. (c) In conventional nonlocal metagratings, larger grating spacing can lead to stronger coupling into higher-order diffraction orders near the THF, reducing the power directed into the desired zeroth-order radiative response and resulting in weaker collected THG. (d) Our proposed ternary dual-resonant design, featuring smaller parent-lattice spacing, reduces coupling into unwanted higher-order diffraction orders, thereby favoring the desired THF radiative response and improving THG outcoupling.

the reduced FBZ, thus reshaping which resonant states become available near the $\Gamma$ point. Notably, the mapping of band-edge features differs for even and odd folding orders: for even $m$, the band-edge features and the associated gap at the boundary of the original FBZ fold to the $\Gamma$ point, whereas for odd $m$ they are mapped to the reduced-FBZ boundary. Higher-order folding can also reposition steeper dispersion segments within the reduced FBZ, as shown in Fig. 2(c) compared with Fig. 2(b), thereby enhancing spectral tunability and expanding the set of $\Gamma$-accessible resonances relevant to multi-resonant nonlinear frequency conversion [37, 38]. In this work, we use the ternary structure as an effective realization of higher-order zone folding. Extending the folding order further, for example to quaternary or quinary configurations, could provide an even richer $\Gamma$-accessible modal landscape. The accompanying reduction in parent-lattice spacing may also reduce coupling into unwanted higher-order diffraction orders more effectively, providing additional flexibility for resonance engineering at harmonic orders beyond third order. Together, these features highlight the potential of the present design strategy for higher-order nonlinear frequency conversion.

Motivated by the greater design flexibility offered by higher-order BZF, we use a ternary metagrating as practical platform to realize the proposed dual-resonant operation. Fig. 1(d) presents the artistic illustration of the ternary metagrating. The structure is implemented using crystalline silicon (c-Si) as the slab and grating material due to its excellent third-order nonlinear susceptibility, $\chi^{(3)} = 2.45 \times 10^{-16}\,(\mathrm{m/V})^2$ as reported in [6]. Substrate ($Al_2O_3$) refractive index was taken as 1.75, while the refractive index of silicon was measured by ellipsometry and is provided in Fig. S2(d). The proposed ternary metagrating originates from the parent unary metagrating, as shown in Fig. 2(a), consisting of an array of silicon gratings patterned on top of a slab, with geometric parameters $P = 178\,\mathrm{nm}$, $h_1 = 100\,\mathrm{nm}$, $h_2 = 200\,\mathrm{nm}$ and $w = 70\,\mathrm{nm}$ denoting the period of the unit cell, grating thickness, slab thickness, and grating width, respectively. Dispersion relations of the modes supported by the unary and ternary metagratings were calculated using eigenmode analysis in COMSOL Multiphysics. In its unperturbed form, the parent unary grating-slab structure supports a well-defined set of GMs (blue), as shown by the band analysis in Fig. 3(a). These modes are nonradiative under ideal periodic conditions and therefore remain confined within the struc-

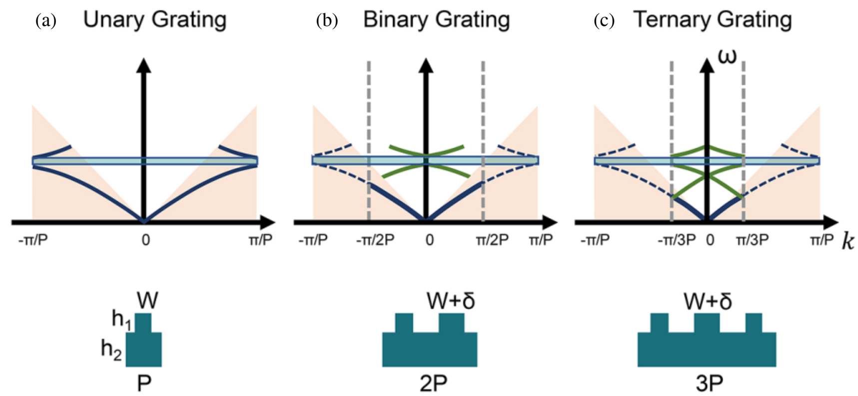


**FIGURE 2**. Schematic illustration of dispersion band variation for different folding orders $mP$ ($m = 1, 2, 3$) (a) Unary metagrating with period P. (b) Binary metagrating with period 2P. (c) Ternary metagrating with period 3P. By adding the perturbation ($\delta$) to every $m$-th element, the unit-cell period increases, and the narrower FBZ folds additional bands into the reduced zone.

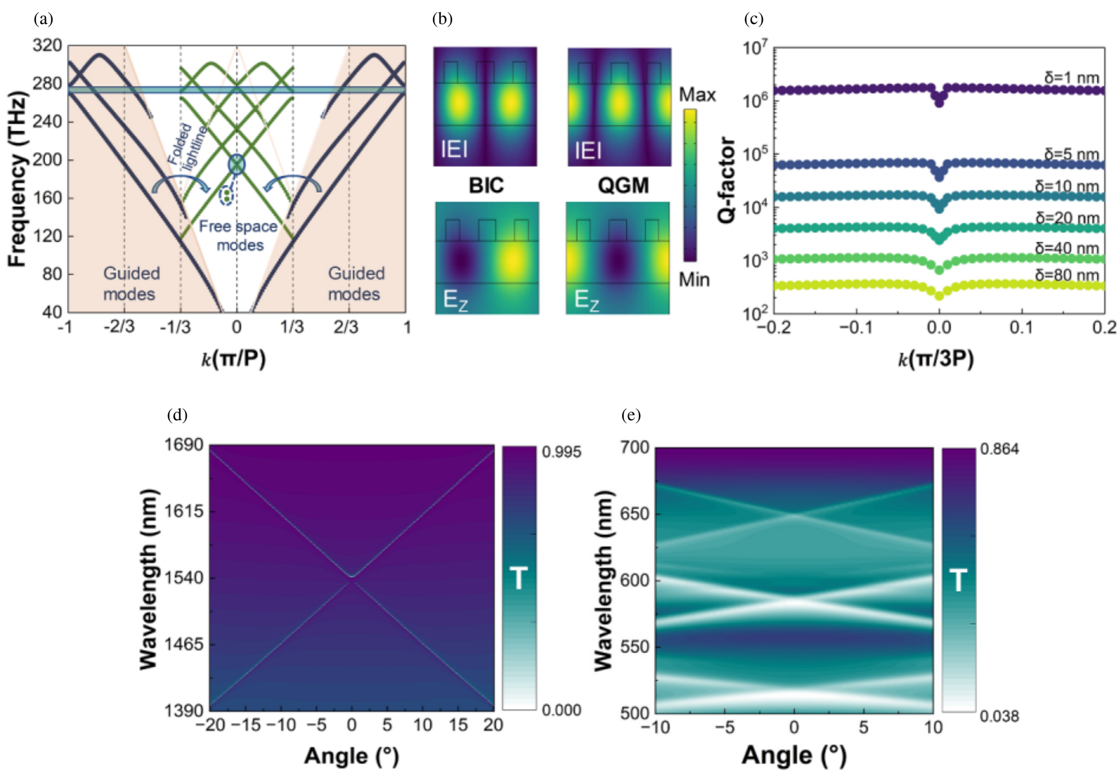


**FIGURE 3**. Dispersion band diagram, field distributions, Q-factors and spectral analysis. (a) Calculated dispersion band diagram for the original unary metagrating (GMs: blue) and ternary metagrating (folded modes: green) with $\delta = 20$ nm. The light-pink shaded area denotes the area below the substrate lightline. (b) Electric-field distributions in the $xz$-plane for two folded modes (left: symmetry-protected BIC and right: QGM), indicated by the cyan ovals in panel (a). (c) Variation of the Q-factor along the wavevector $k$, for different values of $\delta$, transitioning toward the GM limit as $\delta$ approaches zero. (d) Calculated angle-resolved transmission spectra in the FF range for $\pm 20°$ (for the modes in panel (b)) and (e) THF range for $\pm 10°$.

ture without coupling to free-space channels. The light-pink shaded region denotes the area below the substrate light line, and these GMs provide the underlying modal framework from which the folded resonances of the ternary metagrating are derived. When the translational symmetry of the unary grating is intentionally broken by increasing the size of the middle grating in each three-element unit cell by a perturbation $\delta = 20$ nm, a ternary metagrating (3P) is formed. This perturbation folds GM branches, which were originally inaccessible under free-space excitation, into the reduced FBZ and opens controlled coupling pathways to free-space radiation. This controlled redistribution of modal accessibility forms the basis of the present metasurface design and is central to the nonlinear enhancement strategy developed in this paper.

The folding-induced redistribution of resonant states is directly reflected in the calculated band structure (denoted by green color in Fig. 3(a)) of the ternary metagrating (unit cell) shown in Fig. 2(c). The radiative accessibility of these modes arises from the BZF when the primitive period $P$ of the unary grating is expanded to the ternary period $mP = 3P$. This reduces the FBZ to $[-\pi/3P, \pi/3P]$, and the bands of the parent unary lattice are folded into the reduced zone through reciprocal-lattice translation with $G_m = 2\pi/mP$. Consequently, mode segments originally located away from $\Gamma$ become $\Gamma$-accessible after folding, which is particularly advantageous for normal-incidence operations. For ternary folding, the spectral gap associated with the original unary FBZ boundary is mapped to the reduced-FBZ boundary at $k = \pm\pi/3P$ rather than being folded to $\Gamma$, as indicated by the cyan shaded box in Fig. 3(a). A slight shift of folded bands relative to the parent unary dispersion is also observed, originating from the perturbation-induced modification of the effective refractive index [44]. Meanwhile, GM dispersion segments originally located near $k = \pm 2\pi/3P$, often corresponding to a steeper portion of the parent GM band, are folded to $\Gamma$. This redistribution enriches the $\Gamma$-accessible dispersion landscape by placing steeper and more tunable dispersion features directly at normal incidence while relocating the original band-edge gap away from $\Gamma$ [42, 43]. This folding strategy is especially valuable for nonlinear frequency conversion because it increases the number of practically accessible resonances without relying on extreme-Q or fragile slow-light operations.

The folded states at the $\Gamma$ point in Fig. 3(a), denoted by cyan ovals, show two distinct radiative characteristics, which are particularly relevant to this work: QGM and BIC. Despite their common GM origin, the two folded states marked by the cyan circles in Fig. 3(a) exhibit different radiative behaviors near $\Gamma$. Due to the field symmetry at the $\Gamma$ point, one of the states remains embedded in the radiation continuum while its far-field coupling vanishes because of symmetry incompatibility, whereas the other appears as an accessible QGM. The near electric-field profiles of $|E|$ and the real part of $E_z$ in the $xz$-cross-section of these two modes, shown in Fig. 3(b), provide further insight into this behavior. In both cases, the fields remain strongly confined within the nonlinear material, making these modes particularly relevant for nonlinear optical processes. Under controlled perturbation or nonzero incidence angle, the BIC's exact symmetry can be weakly lifted, producing a QBIC with a finite radiative linewidth [12, 25, 29, 41]. The coexistence of QGMs and QBIC-like states in the folded ternary structure therefore provides a useful modal landscape for engineering resonances with distinct radiative characters near the $\Gamma$-point. For the present design, we primarily focus on the QGM because it combines direct free-space accessibility with greater robustness against perturbation-induced spectral shifts than the more symmetry-sensitive QBIC-like mode. Fig. 3(c) shows the evolution of the Q-factor of the selected QGM in momentum space as a function of the size perturbation ($\delta$). This robust behaviour provides the basis for choosing an appropriate perturbation strength as a practical compromise between radiative accessibility and resonance quality. For the selected size perturbation of 20 nm, the simulated radiative Q-factor of the pump-side QGM at the $\Gamma$ point is approximately 2200, corresponding to a spectral linewidth of about 0.70 nm, see Fig. S3 of supporting information for details. In our implementation, the ternary metagrating is realized through a size perturbation of 20 nm for fabrication simplicity, repeatability, and compatibility with a standard lithography and dry-etch process flow.

Next, we calculated the wavelength-angular dispersion of the proposed metagrating near the fundamental and third-harmonic (TH) spectral ranges, with the incident plane oriented parallel to the grating direction ($z$-direction). For simplicity, only TE modes are considered moving forward. In both the fundamental and TH spectral ranges, the red- and blue-shifting resonances, moving away from the $\Gamma$ point, produce a rich, tunable modal landscape over the investigated angular range. Near the fundamental range, these resonances remained relatively close in wavelength while evolving steeply with the angle over $\pm 20°$, allowing the modes to be tuned across a broad spectral window spanning approximately 300 nm (1390–1690 nm). This behavior provides useful tolerance against fabrication-induced spectral offsets and offers a practical route for resonance recovery in experiment. In particular, the closely spaced folded branches within this wavelength range allow small thickness deviations to be compensated by angular shift. In the TH spectral range, a similar dispersive nature is observed for the GMR, QGM, and QBIC modes for $\pm 10°$, over approximately 500-700 nm, offering greater flexibility for $\omega$–$3\omega$ resonance alignment. Here, the $3\omega$ feature is identified as a leaky GMR of the grating-slab structure. The high-index silicon slab supports guided-like modes, while the periodic grating supplies the in-plane momentum required to couple these modes to free-space radiation. Fig. S6 in the Supporting Information further verifies the origin of this harmonic-side resonance by comparing the transmission spectra of slab-only, unperturbed metagrating, and perturbed ternary metagrating structures. This $3\omega$ resonance mainly serves as a radiative outcoupling channel for extracting the generated third-harmonic field into the collected far field, whereas the pump-side resonance at $\omega$ dominates the nonlinear source enhancement. Together, the accessible resonances at $\omega$ and $3\omega$ allow the structure to enhance nonlinear polarization generation while improving far-field extraction of the generated third-harmonic signal.

The proposed ternary metagrating structure supports a rich set of resonances at both the fundamental and TH spectral ranges, as shown in Figs. 3(d) and (e). However, efficient THG extraction also requires that the TH resonance couples predominantly to the zeroth-order radiative channel rather than leaking into higher diffraction orders. As shown schematically in Figs. 1(c) and (d), the reduced grating spacing of the ternary design is advantageous in this regard. Fig. 4 further clarifies this via comparison with binary counterparts under similar conditions. For a fair comparison, three structures (one ternary and two binary metagratings) were designed to have similar Q-factors at similar FF for similar mode profiles. Under similar slab thickness and grating parameters, a binary structure generally requires a larger period than the ternary design to resonate at the same FF, which makes it more difficult to maintain subwavelength grating spacing with respect to the THF. Conversely, if the period is kept comparable to that of the ternary design, the slab thickness must be increased to compensate for the resulting spectral shift. As shown in Figs. 4(a) and (b), the perturbed unit-cell period of both the ternary structure and

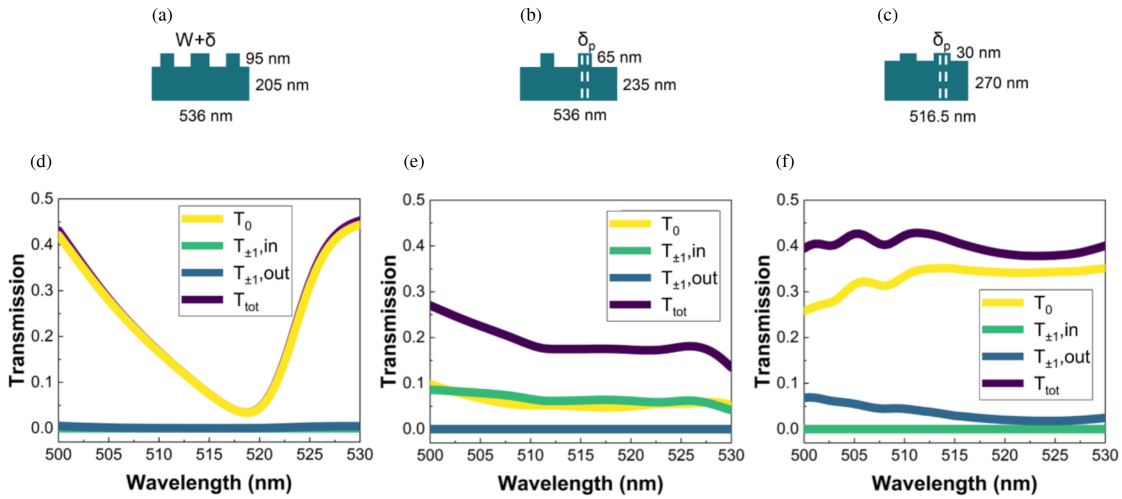


**FIGURE 4**. Diffraction-order decomposition of transmittance in ternary and binary metagratings in the TH range. (a) Ternary metagrating unit cell with reduced grating spacing, with the corresponding diffraction response in (d) showing a well-defined TH resonance with weak coupling to higher-order diffraction channels. (b) Binary metagrating with a period similar to that in panel (a), with the corresponding diffraction response in (e) showing stronger coupling to higher-order diffraction channels in the TH range. (c) Binary metagrating with a period further reduced compared with (a), (b), with the corresponding diffraction response in (f) showing reduced coupling to higher diffraction channels compared with the binary metagrating in panel (b). Both binary metagratings (b), (e) and (c), (f) fall short of a well-defined resonance in the TH range. Here, $T_0$ denotes the zeroth-order transmittance, while $T_{\pm1}$,in and $T_{\pm1}$, out denote the in-plane and out-of-plane polarization components, respectively, of the $\pm1$ diffraction-order transmittance, defined with respect to the diffraction plane. Under the present normal-incidence configuration, the calculated $+1$ and $-1$ orders are identical and therefore overlap in the plotted curves.

one binary structure was fixed at 536 nm, while the total silicon thickness was maintained at 300 nm throughout the study. Under these conditions, the larger grating spacing in the binary design leads to stronger coupling into the allowed higher-order diffraction orders near the TH wavelength range ($\sim$ 500–530 nm), redirecting power away from the desired zeroth-order response and thereby weakening THG outcoupling [45–47]. The existence of propagating diffraction channels is determined by the full supercell period, together with the wavelength, incidence angle, and refractive index of the output medium. Although the smaller parent-lattice spacing does not close these diffraction channels, it may reduce coupling into the allowed higher-order diffraction orders, as shown in Figs. 4(d)–(f).

To extend this comparison, the period of the second binary structure was further reduced, as shown in Fig. 4(c), and the slab thickness was correspondingly increased to compensate for the resulting spectral shift. This modified binary design, with a period of 516.5 nm, was used as an additional benchmark against the ternary structure. Although this period reduction and slab thickness adjustment help mitigate higher-order diffraction to some extent, the binary structures still exhibit stronger coupling into higher-order diffraction orders because of their larger grating spacing. Consequently, a significant portion of the TH energy is radiated into unwanted diffraction orders rather than being efficiently coupled into the dominant radiative channel near normal incidence [5, 45, 47]. Within the fabrication-compatible design space examined in this work, the ternary metagrating provides more favorable simultaneous matching of the pump-side resonance and the harmonic-side radiative response than the specific binary designs considered here. This comparison is limited to the examined binary structures and folded mode branches, and does not exclude the possibility that other carefully optimized binary metagratings may also achieve dual-resonant THG performance under different geometric, material, or spectral conditions.

To further validate the robustness of our design and compare the THG performance of the ternary metagrating with that of the binary counterpart, we examined the response of both structures (ternary: Fig. 4(a) and binary: Fig. 4(c)) under geometric perturbations and thickness variations. Specifically, size modulation was applied to the ternary structure, whereas position perturbation was introduced in the binary structure to access a similar mode profile, as shown in the insets of Figs. 5(a) and (d). This highlights that comparable mode profiles in different structures may originate from different symmetry properties and therefore require distinct perturbation strategies. Both structures were subjected to varying perturbation extents to calculate the corresponding changes in their pump-side Q-factors, as shown in Figs. 5(a) and (d), providing valuable insight into their stability and resonance behavior under different levels of geometric modification. This allowed us to assess the resilience of each structure to geometric variations and control the Q-factor for a fair comparison in the subsequent analysis.

We then evaluated the spectral tolerance of the ternary structure in Fig. 4(a) as a function of perturbation strength and grating thickness and compared it with that of the binary design in Fig. 4(c). The corresponding 2D spectral maps are shown in Figs. 5(b), (c), (e), and (f), where the black dots overlaid on each map indicate the expected TH wavelength relative to the designed fundamental resonance wavelength under the applied perturbation. As shown in Figs. 5(b) and (c), the ternary structure supports a well-defined zeroth-order resonance over

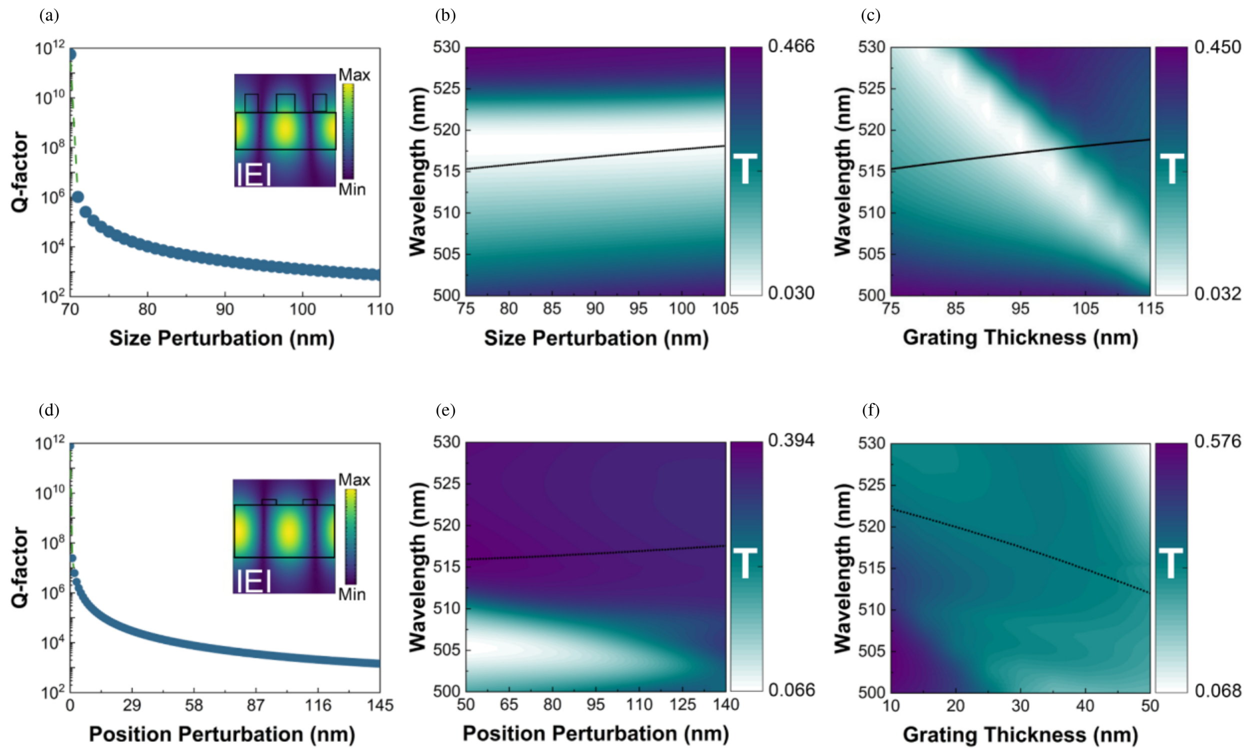


**FIGURE 5**. Q-factor and spectral robustness under geometric perturbations. (a) Calculated Q-factor of the ternary metagrating as a function of size perturbation and (d) of the binary structure as a function of position perturbation, using the same structural parameters as in Figs. 4(a), (c), respectively. Insets show the respective electric field profiles at the FF. (b) The simulated transmission spectral maps highlighting the resonance evolution as a function of perturbation and grating thickness for the ternary (b), (c) and binary metagratings (e), (f). Black dots indicate the expected TH wavelength corresponding to fundamental resonance.

nearly the entire perturbation range and remains closely aligned with the expected position of the THG. In contrast, the binary structure in Figs. 5(e) and (f) show little to no overlapping pronounced zeroth-order resonance. When the grating thickness is varied, the ternary resonance shifts only slightly and remains well-aligned with the targeted TH resonance position over most of the thickness range, indicating excellent tolerance to parametric variation or deviation under practical conditions. This result shows that the ternary structure can preserve the resonance alignment required for dual-resonant operation, even in the presence of modest fabrication imperfections. Overall, these results confirm that the ternary design offers a substantially robust platform for dual-resonant THG, maintaining the required resonance alignment across a broad parameter space, whereas the binary counterpart fails to provide a comparable and effective radiative channel.

In light of these findings, we numerically evaluated the THG performance of the dual and single resonant structures, treating the ternary structure as dual-resonant and the binary structure as single-resonant. To ensure a fair comparison, the binary reference structure was selected to provide a pump-side resonance comparable to that of the ternary design. Specifically, the resonance wavelength, Q-factor, and fundamental-field mode profile at $\omega$ were closely matched, as indicated by the field profiles in the insets of Figs. 5(a) and (d) and further quantified in Table S1 of the Supporting Information. Therefore, the difference in behaviour at $3\omega$ is a reflection of the intrinsic difference in harmonic-side radiative characteristics between the two designs under discussion. It is worth noting that the binary structure can still support a weak TH resonance in the spectral range of interest, but its contrast is very low ($\sim 0.01$). Although this resonance contributes to the THG response in simulations, it would be highly susceptible to losses and experimental imperfections under realistic conditions, which would significantly reduce or even eliminate its practical contribution. Nevertheless, the electric-field profiles supported by both structures in the visible range of interest at three representative Q-factors are shown in Figs. 6(a)–(c) for the ternary structure and Figs. 6(d)–(f) for the binary structure. Next, we calculated the THG conversion efficiency ($P_{THG}/P_{in}$) by exciting the metasurface with a monochromatic FF wave at an intensity of 5.49 MW/cm$^{-2}$, chosen to better reflect realistic experimental conditions. THG conversion efficiency shown in Fig. 6(g) was determined by integrating the output TH power at the output surface for Q-factors ranging from 1500 to 10,500. Nonlinear THG simulation was performed using a perturbative frequency-domain source method under the undepleted-pump approximation. The pump field at $\omega$ was first calculated linearly, and the generated third-order nonlinear polarization in silicon was then used as an equivalent source at $3\omega$. Floquet periodic boundary conditions were applied laterally, and perfectly matched layers were used in the vertical direction. Radiated THG power was obtained by integrating the time-averaged Poynting vector at $3\omega$ over output monitor planes. Full details of equiv-

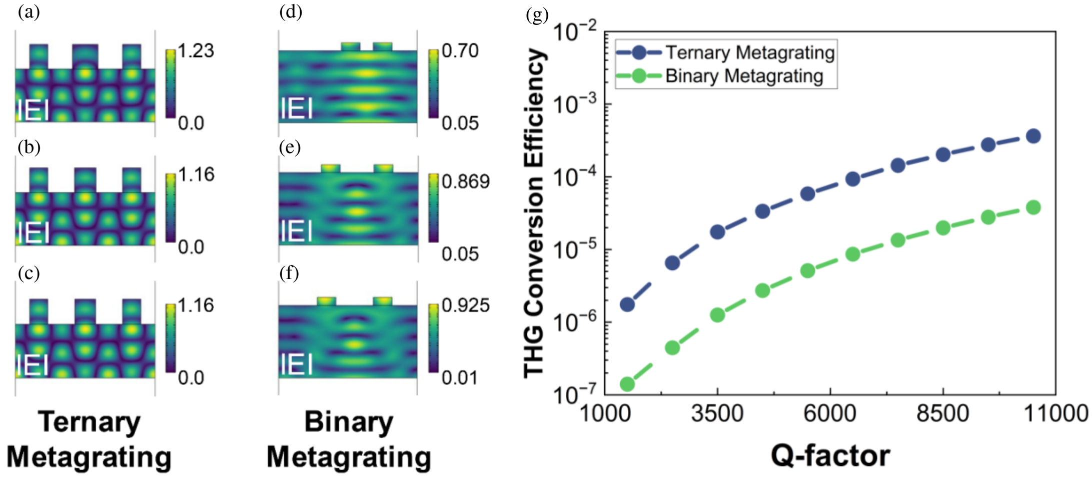


**FIGURE 6**. Electric-field distributions and THG conversion efficiency of ternary and binary metagratings. (a)–(f) Electric field profiles for three representative Q-factors (1500, 5500 and 10500) for the ternary (a)–(c) and binary (d)–(f) metagratings at the TH resonance. (g) Calculated THG conversion efficiency as a function of Q-factor, demonstrating ternary metagrating's consistent superiority over the binary metagrating across the entire Q-factor range, by at least one order of magnitude.

alent nonlinear current-source implementation, $\chi^{(3)}$ assumptions, monitor-plane placement, mesh-convergence procedure, and Q-factor extraction method are provided in Section III of the Supporting Information.

For similar pump-side Q-factors and comparable fundamental wavelengths, the ternary structure shows at least an order-of-magnitude higher calculated THG conversion efficiency than the specific binary structure considered in this work. This improvement arises primarily from the dual-resonant condition, where pump-side field enhancement at $\omega$ is combined with a more favourable radiative outcoupling channel near $3\omega$. Therefore, the comparison should be understood as a design-specific result within the examined fabrication-compatible parameter space, rather than as a universal conclusion that ternary metagratings must always outperform binary metagratings. The same physical principle may also apply to other binary or alternative metasurface geometries if they are engineered to provide simultaneous resonance matching at the pump and harmonic frequencies.

After establishing superior performance of the ternary metagrating, we proceeded to experimentally validate the proposed structure using previously discussed optimized geometric parameters. The proposed silicon metagrating was fabricated using standard nanofabrication techniques, specifically electron-beam lithography (EBL) and inductively coupled plasma reactive-ion etching (ICP-RIE), to precisely define the patterned gratings and accurately control the etch depth. Fig. S1 provides full fabrication details. The SEM image of the fabricated sample (Fig. 7(a)) reveals high structural quality, with the inset providing a magnified view; the yellow scale bars correspond to 200 nm and 1 $\mu$m, respectively. Subsequently, we characterized the linear and nonlinear optical responses of the fabricated device using a home-built optical setup, as shown in Fig. S9. Fig. 7(b) shows the experimentally measured angle-resolved transmission map in the fundamental spectral range under $z$-polarized illumination over an angular range of $\pm 20°$.

The measured map captures the overall dispersive behavior of folded modes and shows good agreement with simulated results, shown in Fig. 3(d), confirming that the main resonant features are well retained after fabrication. To further provide a quantitative evaluation of the resonance linewidth and Q-factor at normal incidence, Fig. S3(b) shows a conventional one-dimensional transmission spectrum. The experimental spectrum exhibits a clear Fano-type resonance dip around 1548 nm, consistent with the simulated Fano resonance shown in Fig. S3(a). Fano fitting of the experimental spectrum in Fig. S3(b) gives an experimental Q-factor of approximately 750, corresponding to a linewidth of about 2.1 nm. This confirms the experimental observation of the targeted QGM resonance near the Γ point. A symmetry-protected BIC mode, non-radiative at the Γ point, manifests as a QBIC under oblique incidence and shows a clear blueshift with increasing angle, in stark contrast to the QGM branch, which displays a distinct redshifting nature. Over the mapped angular range of $\pm 20°$, these two modes together span an approximate wavelength range of 1390–1690 nm, corresponding to a spectral coverage of approximately 300 nm. This broad tuning range arises from the strongly dispersive nature introduced by the higher-order BZF, which is particularly advantageous for $\omega$-$3\omega$ resonance matching. Toward shorter wavelengths near 1390 nm, silicon's optical loss begins to dominate slightly, whereas toward longer wavelengths the resonance approaches the upper detection limit of our spectrometer at 1700 nm, leading to a gradual decrease in the signal-to-noise ratio. Nevertheless, the measured modes provide a broad and practically useful tuning window. Overall, good qualitative agreement was achieved between the simulation and experiment in resonant behaviour, supporting the successful realization of the intended high-Q resonance. A minor spectral shift and a slightly reduced Q-factor were observed experimentally relative to the numerical design, which can be attributed to small fabrication-induced deviations in etch depth, grating width, slab thickness, or minor uncertainties in the refractive index and loss values used in the simulations.

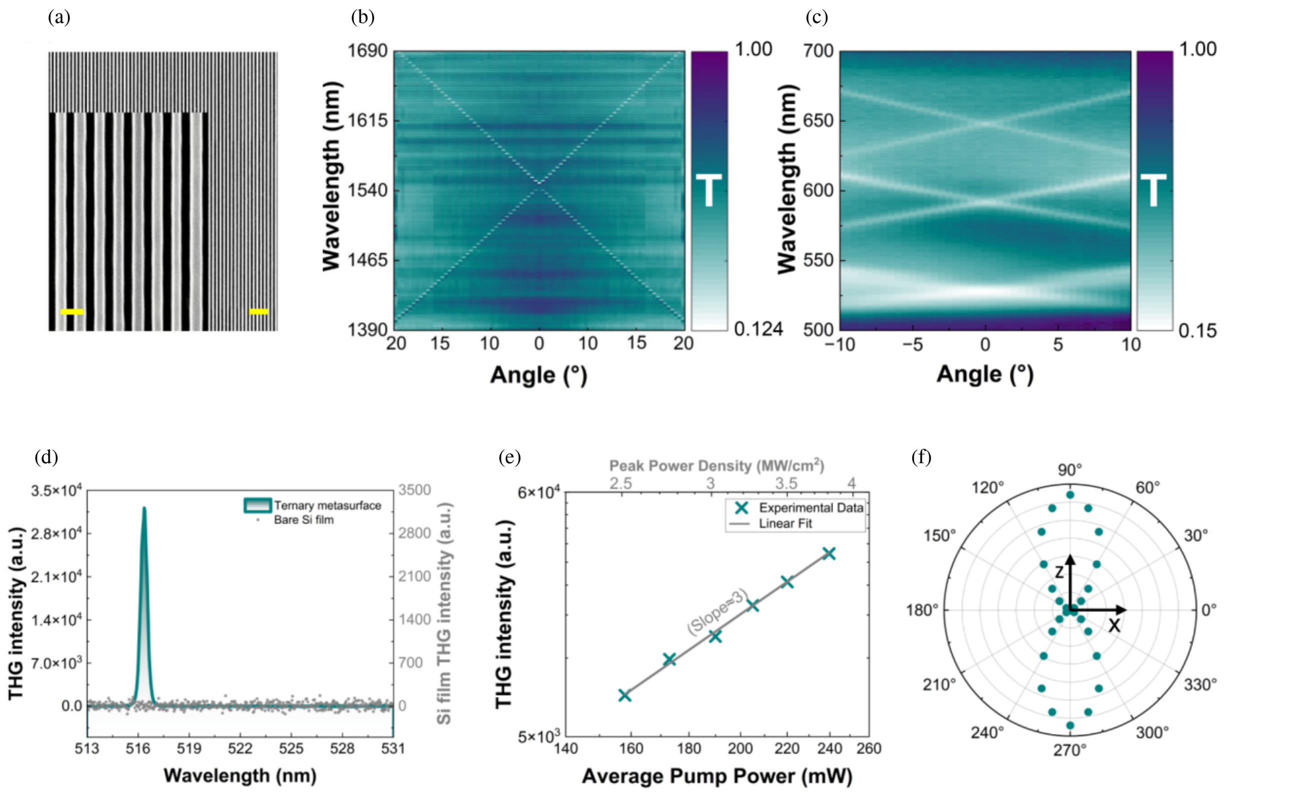


**FIGURE 7**. Structural and optical characterization of the fabricated ternary metagrating. (a) SEM image of the fabricated ternary metagrating. The yellow scale bars represent 200 nm and 1 µm, respectively. (b) 2D wavelength-angle transmission map near the FF and (c) THF, showing the rich and dispersive mode profile of the ternary metagrating. (d) Measured THG signal spectra from the ternary metagrating and bare silicon film denoted by cyan and gray colours, respectively. (e) Log-log plot of THG intensity as a function of average pump power, with experimental data (cyan crosses) and linear fit (gray line). (f) Polar plot of the THG intensity measured under various pump polarizations. The pump polarization was varied by rotating the half-wave plate in the incident pump path, while the THG collection path remained fixed. The angular coordinate represents the incident pump-polarization angle relative to the grating direction, while the radial coordinate represents the measured THG signal, with a scale ranging from 0 to $3.5 \times 10^4$.

Next, we characterized the angle-resolved transmission map in the TH spectral range under $z$-polarized illumination. A strongly dispersive, rich modal landscape was observed in the 500–700 nm range across an angular sweep of $\pm 10°$. The experimentally measured transmission map reproduces the main simulated dispersive features, including the primary resonance branch and a narrower angle-activated mode away from normal incidence, which is consistent with a BIC-type mode whose radiative coupling is suppressed near $\theta \approx 0°$ and gradually opens under tilted excitation. The third-harmonic-frequency resonance was refitted using a Fano line shape, giving an experimental Q-factor of approximately 25, as shown in Fig. S5 of the Supporting Information. This value is in reasonable agreement with the simulated harmonic-side resonance, and the small remaining difference can be attributed to fabrication tolerances, visible-range optical-constant uncertainty, finite angular spread, and measurement resolution. At the third-harmonic wavelength, silicon absorption is non-negligible and imposes an absorption-limited upper bound on the harmonic-side Q-factor. From the fitted resonance using the measured visible-range extinction coefficient, together with the corresponding $k = 0$ reference case, we estimate $Q_{abs} \approx 46$ near $3\omega$, see Fig. S4 of the Supporting Information for details. This indicates that material absorption significantly limits the total Q-factor; therefore, further increasing $Q_{rad}$ at $3\omega$ would provide only limited improvement in $Q_{tot}$. Thus, the $3\omega$ resonance is best understood as a moderate-Q radiative outcoupling channel for efficient THG extraction, rather than as an ultra-high-Q storage mode.

The appearance of an angle-activated QBIC together with experimentally observed Q-factors of approximately 25, 98, and 150 for different Γ-accessible resonances in the THF range further confirms that the ternary folded platform provides additional degrees of freedom for resonance alignment through modest angle tuning. Importantly, despite the slight spectral mismatch between the simulated and measured transmission spectra, excellent $\omega$-$3\omega$ spectral matching was still preserved, which is sufficient for practical dual-resonant operation and efficient TH outcoupling. Fig. S7 and Fig. S8 further discuss the impact of more precise $\omega$-$3\omega$ matching. Nevertheless, the observed TH-side resonances remain particularly valuable for recovering resonance alignment in the presence of fabrication-induced imperfections.

Having experimentally validated linear resonant features of the fabricated device, we next evaluated its nonlinear response through THG measurements under nanosecond laser excitation. The pump wavelength was tuned such that the generated THG fell within the 500–540 nm detection window. The emitted THG was collected from the substrate side and spectrally recorded, with further details provided in Fig. S9. For the measurements in Figs. 7(d)–(f), the pump wavelength was 1548 nm; the pulse duration was 20 ns; the repetition rate was 10 kHz; the incident average pump power was 240 mW; the pump spot diameter was approximately 200 μm; and the estimated peak and average intensities were 3.82 MW cm$^{-2}$ and 764 W cm$^{-2}$, respectively. The pump was $z$-polarized along the grating direction, and the measurements were performed at normal incidence. The THG signal was collected using a 20× objective with $NA = 0.5$; the residual pump was removed using optical filters, and dark-background subtraction was applied before spectral analysis. The detector response was within the linear regime, and the spectrometer calibration used to estimate the collected THG power and external collected THG conversion efficiency is provided in Section IX of the Supporting Information.

Fig. 7(d) shows collected THG spectra from both the fabricated ternary metagrating and an unpatterned bare silicon film of comparable thickness measured under identical optical configuration. Due to the intrinsically low THG efficiency of the bare silicon film under these conditions, its signal remains close to the background and exhibits no resolvable resonance-associated peak. In striking contrast, a pronounced and spectrally localized THG peak is observed from the metagrating. This direct comparison confirms that the strong harmonic emission does not arise simply from the intrinsic $\chi^{(3)}$ nonlinearity of silicon, but from the engineered photonic environment of the ternary structure, which simultaneously enhances the nonlinear interaction and promotes efficient far-field radiation of the generated harmonic. Under a pump power of 240 mW, the metasurface produces a THG signal exceeding $3.2 \times 10^4$ a.u., conclusively demonstrating the practical advantage of dual-resonant operation. The dual-resonant THG enhancement arises from the combined effect of pump-side field build-up and harmonic-side radiative extraction. In the perturbative regime, $P^{(3)}(3\omega) \propto E(\omega)^{(3)}$, so the resonance at $\omega$ strengthens the nonlinear source [6], while the resonance near 3$\omega$ provides an outcoupling channel for the generated harmonic field. This can be expressed qualitatively as $I_{3\omega}^{out} \propto |L_\omega|^6 \left|\hat{G}(3\omega)\right|^2$, where $L_\omega$ denotes the local pump-field enhancement factor, and $\hat{G}(3\omega)$ represents the harmonic-side response, including radiative outcoupling of the generated third-harmonic field [32]. In our fabricated device, $Q_\omega \approx 750$ and $Q_{3\omega} \approx 25$, leading to a collected THG power of approximately 0.45 μW and an estimated collected conversion efficiency of approximately $1.86 \times 10^{-6}$. The experimentally measured THG signal from the ternary metagrating exceeds $3.2 \times 10^4$ a.u. At the corresponding THG wavelength, the bare-Si spectral intensity remains within the detector-background fluctuations. Even when the maximum bare-Si spectral intensity over the entire 500–530 nm range is adopted as a conservative upper bound, the noise-referenced THG enhancement remains greater than $10^2$ (see Section IX of the Supporting Information for the detailed lower-bound analysis).

We further investigated the power dependence of THG signal to verify its nonlinear origin. As shown in Fig. 7(e), the THG intensity increases cubically with pump power, precisely as expected for a third-order nonlinear process. A linear fit on log-log axes yields a slope of approximately 3, in excellent agreement with the relation $I_{3\omega} \propto P\omega^3$. Two-photon absorption, free-carrier absorption, and thermal effects were not explicitly included in simulations; these effects are considered secondary under present conditions because the measured THG response remained cubic without clear saturation, resonance drift, or sample damage over the investigated power range [48, 49]. We also examined the dependence of the THG intensity on the incident pump polarization, as shown in Fig. 7(f). For this measurement, the half-wave plate in the incident pump path was rotated to vary the pump polarization before the sample, while the THG collection path remained fixed. The angular coordinate in Fig. 7(f) represents the incident pump-polarization angle relative to the grating direction. Because the structure breaks in-plane symmetry and supports polarization-selective resonant fields, the resonant excitation and induced nonlinear polarization depend strongly on the incident pump-polarization direction, producing the lobed THG intensity pattern observed experimentally.

These measurements reinforce an important physical conclusion: strong externally collected THG is not determined by Q alone. While a high-Q resonance at $\omega$ certainly enhances the driving fundamental field, the detected THG signal also depends critically on whether the generated harmonic signal can be efficiently radiated through a suitable 3$\omega$ channel. Consequently, a well-matched radiative resonance at the THF can provide efficient harmonic outcoupling and offer advantages over approaches that rely only on a single resonance or on very high-Q flat-band states whose outcoupling is not optimized for external collection. Compared with closely related high-Q THG measurements based on 300-nm-thick silicon metasurfaces under similar nanosecond-OPO excitation and collection configurations, the present dual-resonant ternary metagrating shows a stronger collected THG response, as summarized in Table S4. This highlights the practical benefit of combining pump-side field enhancement with harmonic-side radiative outcoupling in a single experimentally realized platform [6, 12]. More generally, the Brillouin-zone-folding strategy provides a modal-engineering route beyond the present ternary silicon metagrating. By introducing an m-fold superperiodic perturbation, the Brillouin zone is reduced, and guided-mode branches are folded toward the $\Gamma$ point, enabling additional radiative resonances. Higher-order folding can also preserve a smaller parent-lattice period, maintaining a deeply subwavelength grating while increasing modal flexibility, although the resulting diffraction behavior must still be evaluated for the full structure. This approach can be extended to other folding orders, dielectric platforms, and nonlinear processes where dual-resonant matching is achievable, as well as to different applications. For example, in Raman metasurfaces it can improve simultaneous excitation and Stokes enhancement [50], and in thermal emitters it can improve emission directionality via folded dispersion engineering [42].

Nevertheless, efficient nonlinear conversion requires simultaneous optimization of resonance alignment, Q-factors, modal overlap, and radiation channels. More broadly, independent control of both resonances, such as by employing two-dimensional devices or flat-band-assisted [6, 19, 24, 51] dual-resonant architectures, may further enhance light-matter interaction and nonlinear frequency conversion. Therefore, the present design should be viewed as a flexible dual-resonant platform rather than a universal solution, and these concepts may be further extended in future to more flexible geometries and multi-resonant metasurface systems.

## 3. CONCLUSION

To summarize, by achieving dual-resonant spectral matching between a quasi-guided mode at $\omega$ (for efficient field build-up) and a guided-mode resonance at $3\omega$ (for efficient outcoupling), we enable THG in a ternary metagrating on a silicon-on-sapphire platform. The period-tripled structure with reduced Brillouin zone facilitates steeper dispersion, a smaller spectral gap, and a richer $\Gamma$-accessible modal landscape. Consequently, we observe broad tunability: the folded QGM and off-normal quasi-BIC span approximately 300 nm over $\pm 20°$ near $\omega$, while visible resonances cover 500–700 nm over $\pm 10°$ at $3\omega$, with experimentally observed Q-factors reaching approximately 750 at $\omega$ and 25 at $3\omega$. Numerically, within the fabrication-compatible design space examined here, the ternary structure outperforms binary counterparts under identical conditions by at least an order of magnitude in THG conversion efficiency, with lower diffraction leakage and superior tunability. Experimentally, our ternary dual-resonant metasurface demonstrated a strong THG signal and an estimated collected THG conversion efficiency of approximately $1.86 \times 10^{-6}$, attributed to robust $\omega$–$3\omega$ matching. This conversion efficiency is comparable to or even higher than previously reported flat-band and ultrahigh-Q single-resonant structures measured under closely related excitation and collection conditions. Together, these results establish the dual-resonant ternary metagrating as a practical, fabrication-friendly architecture for strong THG enhancement, opening new avenues for sensing, imaging, communications, and quantum technologies.

## REFERENCES


[1] Li, Y., S. H. Wang, B. E. Little, and S. T. Chu, "High harmonic generation in integrated nonlinear platforms (invited paper)," *Progress In Electromagnetics Research*, Vol. 182, 27–54, 2025.

[2] Singh, S. and A. Forbes, "Progress in structured light with nonlinear optics," *Progress In Electromagnetics Research*, Vol. 185, 1–16, 2026.

[3] Bijloo, F., M. Ogienko, A. J. d. Boef, P. M. Kraus, and A. F. Koenderink, "All-optical nonlinear real and fourier-space shaping with all-dielectric fano resonant metasurfaces," *ACS Nano*, Vol. 20, No. 6, 4845–4854, 2026.

[4] Schlickriede, C., S. S. Kruk, L. Wang, B. Sain, Y. Kivshar, and T. Zentgraf, "Nonlinear imaging with all-dielectric metasurfaces," *Nano letters*, Vol. 20, No. 6, 4370–4376, 2020.

[5] Li, G., S. Zhang, and T. Zentgraf, "Nonlinear photonic metasurfaces," *Nature Reviews Materials*, Vol. 2, 17010, 2017.

[6] Sun, K., K. Wang, W. Wang, Y. Cai, L. Huang, A. Alù, and Z. Han, "High-Q photonic flat-band resonances for enhancing third-harmonic generation in all-dielectric metasurfaces," *Newton*, Vol. 1, No. 4, 100057, 2025.

[7] Yanagimoto, R., B. A. Ash, M. M. Sohoni, M. M. Stein, Y. Zhao, F. Presutti, M. Jankowski, L. G. Wright, T. Onodera, and P. L. McMahon, "Programmable on-chip nonlinear photonics," *Nature*, Vol. 649, 330–337, 2026.

[8] Hail, C. U., L. Michaeli, and H. A. Atwater, "Third harmonic generation enhancement and wavefront control using a local high-Q metasurface," *Nano Letters*, Vol. 24, No. 7, 2257–2263, 2024.

[9] Vabishchevich, P. and Y. Kivshar, "Nonlinear photonics with metasurfaces," *Photonics Research*, Vol. 11, No. 2, B50–B64, 2023.

[10] Krasnok, A., M. Tymchenko, and A. Alù, "Nonlinear metasurfaces: A paradigm shift in nonlinear optics," *Materials Today*, Vol. 21, No. 1, 8–21, 2018.

[11] Duncan, C., L. Perret, S. Palomba, M. Lapine, B. T. Kuhlmey, and C. M. De Sterke, "New avenues for phase matching in nonlinear hyperbolic metamaterials," *Scientific Reports*, Vol. 5, 8983, 2015.

[12] Jiang, H., Y. Cai, and Z. Han, "Enhanced high-harmonic generation with spectral tunability in nonlocal metasurfaces enabled by the excitation of quasiguided modes," *Physical Review B*, Vol. 110, 245424, 2024.

[13] Sinev, I. S., K. Koshelev, Z. Liu, A. Rudenko, K. Ladutenko, A. Shcherbakov, Z. Sadrieva, M. Baranov, T. Itina, J. Liu, A. A. Bogdanov, and Y. Kivshar, "Observation of ultrafast self-action effects in quasi-BIC resonant metasurfaces," *Nano Letters*, Vol. 21, No. 20, 8848–8855, 2021.

[14] Gigli, C. and G. Leo, "All-dielectric χ(2) metasurfaces: Recent progress," *Opto-Electronic Advances*, Vol. 5, No. 7, 210093, 2022.

[15] Yu, N. and F. Capasso, "Flat optics with designer metasurfaces," *Nature Materials*, Vol. 13, 139–150, 2014.

[16] Xun, W., K. Sun, E. Maqbool, and Z. Han, "High-Q chiral metasurfaces: Broadband spectral tunability with angle-dependent response," *Advanced Optical Materials*, Vol. 13, No. 21, 2500713, 2025.

[17] Hähnel, D., C. Golla, M. Albert, T. Zentgraf, V. Myroshnychenko, J. Förstner, and C. Meier, "A multi-mode super-fano mechanism for enhanced third harmonic generation in silicon metasurfaces," *Light: Science & Applications*, Vol. 12, 97, 2023.

[18] Liu, Z., Y. Xu, Y. Lin, J. Xiang, T. Feng, Q. Cao, J. Li, S. Lan, and J. Liu, "High-Q quasibound states in the continuum for nonlinear metasurfaces," *Physical Review Letters*, Vol. 123, 253901, 2019.

[19] Wang, Y., Z. Wang, Y. Deng, L. Wang, P. Xu, J. Cui, C. Y. Leong, C. Yu, and C.-W. Qiu, "Plasmonic flat-band quasi-bound states in the continuum for ultrasensitive fiber-tip sensing," *Laser & Photonics Reviews*, Vol. 20, No. 4, e01247, 2026.

[20] Liang, Y., K. Koshelev, F. Zhang, H. Lin, S. Lin, J. Wu, B. Jia, and Y. Kivshar, "Bound states in the continuum in anisotropic plasmonic metasurfaces," *Nano Letters*, Vol. 20, No. 9, 6351–6356, 2020.

[21] Linnenbank, H., Y. Grynko, J. Förstner, and S. Linden, "Second harmonic generation spectroscopy on hybrid plasmonic/dielectric nanoantennas," *Light: Science & Applications*, Vol. 5, e16013, 2016.

[22] Wu, N., Y. Zhang, H. Ma, H. Chen, and H. Qian, "Tunable high-Q plasmonic metasurface with multiple surface lattice resonances (invited)," *Progress In Electromagnetics Research*, Vol. 172, 23–32, 2021.

[23] Koshelev, K., S. Kruk, E. Melik-Gaykazyan, J.-H. Choi, A. Bogdanov, H.-G. Park, and Y. Kivshar, "Subwavelength dielectric resonators for nonlinear nanophotonics," *Science*, Vol. 367, No. 6475, 288–292, 2020.

[24] Sun, K., Y. Cai, Y. Kivshar, and Z. Han, "Flatband high-Q metasurfaces inspired by coupled-resonator optical waveguides," *Advanced Photonics*, Vol. 7, No. 5, 056008, 2025.

[25] Hsu, C. W., B. Zhen, A. D. Stone, J. D. Joannopoulos, and M. Soljačić, "Bound states in the continuum," *Nature Reviews Materials*, Vol. 1, 16048, 2016.

[26] Aigner, A., A. Tittl, J. Wang, T. Weber, Y. Kivshar, S. A. Maier, and H. Ren, "Plasmonic bound states in the continuum to tailor light-matter coupling," *Science Advances*, Vol. 8, eadd4816, 2022.

[27] Wang, K., K. Sun, J. Du, P. Dai, H. Zhou, L. Huang, Z. Han, and W. Wang, "Cavity-assisted nonlocal metasurfaces for momentum-space broadband-operational optical vortice generation with maximum efficiency approaching 80%," *Opto-Electronic Advances*, Vol. 9, No. 7, 250296, 2026.

[28] Liu, T., J. Qiu, M. Qin, X. Tu, H. Qiu, F. Wu, T. Yu, Q. Liu, and S. Xiao, "High-efficiency infrared upconversion imaging with nonlinear silicon metasurfaces empowered by quasi-bound states in the continuum," *Opto-Electronic Advances*, Vol. 9, 250257, 2026.

[29] Huang, L., R. Jin, C. Zhou, G. Li, L. Xu, A. Overvig, F. Deng, X. Chen, W. Lu, A. Alù, and A. E. Miroshnichenko, "Ultrahigh-Q guided mode resonances in an all-dielectric metasurface," *Nature Communications*, Vol. 14, 3433, 2023.

[30] Rybin, M. V., K. L. Koshelev, Z. F. Sadrieva, K. B. Samusev, A. A. Bogdanov, M. F. Limonov, and Y. S. Kivshar, "High-Q supercavity modes in subwavelength dielectric resonators," *Physical review letters*, Vol. 119, 243901, 2017.

[31] Kang, Z., C. Mei, L. Zhang, Z. Zhang, J. S. G. Evans, Y. Cheng, K. Zhu, X. Zhang, D. Huang, Y. Li, J. He, Q. Wu, B. Yan, K. Wang, X. Zhou, K. Long, F. Li, Q. Li, S. Wang, J. Yuan, P. K. A. Wai, and S. He, "Advanced progress on χ(3) nonlinearity in chip-scale photonic platforms (invited review)," *Progress In Electromagnetics Research*, Vol. 170, 17–62, 2021.

[32] Carletti, L., K. Koshelev, C. D. Angelis, and Y. Kivshar, "Giant nonlinear response at the nanoscale driven by bound states in the continuum," *Physical Review Letters*, Vol. 121, 033903, 2018.

[33] Silvestri, M., A. Sahoo, C. Ferrante, P. Benassi, A. Ciattoni, and A. Marini, "Doubly resonant third-harmonic generation in near-zero-index heterogeneous nanostructures," *Physical Review A*, Vol. 110, 023524, 2024.

[34] You, J. W., J. You, M. Weismann, and N. C. Panoiu, "Double-resonant enhancement of third-harmonic generation in graphene nanostructures," *Philosophical Transactions of the Royal Society A*, Vol. 375, No. 2090, 20160313, 2017.

[35] You, J. W. and N. C. Panoiu, "Tunable and dual-broadband giant enhancement of second-harmonic and third-harmonic generation in an optimized graphene-insulator-graphene metasurface," *Physical Review B*, Vol. 102, 121403(R), 2020.

[36] Thyagarajan, K., S. Rivier, A. Lovera, and O. J. F. Martin, "Enhanced second-harmonic generation from double resonant plasmonic antennae," *Optics Express*, Vol. 20, No. 12, 12 860–12 865, 2012.

[37] Zeng, Y., H. Qian, M. J. Rozin, Z. Liu, and A. R. Tao, "Enhanced second harmonic generation in double-resonance colloidal metasurfaces," *Advanced Functional Materials*, Vol. 28, No. 51, 1803019, 2018.

[38] Ji, M., Z. Qin, H. Chen, T. Hu, Z. Chen, and P. Zhan, "Doubly-resonant enhanced second-harmonic generation and its wide-band tunability," *Optics Communications*, Vol. 539, 129493, 2023.

[39] Wang, C., S. Li, Y. Chen, Q. Zhou, J. Luo, S. Wang, L. Gao, and Y. Xu, "Dual-resonance metagrating for enhancing or annihilating third-harmonic generation at terahertz frequencies," *Physical Review A*, Vol. 111, 063509, 2025.

[40] Liang, Y., D. P. Tsai, and Y. Kivshar, "From local to nonlocal high-Q plasmonic metasurfaces," *Physical Review Letters*, Vol. 133, 053801, 2024.

[41] Overvig, A. C., S. Shrestha, and N. Yu, "Dimerized high contrast gratings," *Nanophotonics*, Vol. 7, No. 6, 1157–1168, 2018.

[42] Sun, K., U. Levy, and Z. Han, "Exploiting zone-folding induced quasi-bound modes to achieve highly coherent thermal emissions," *Nano Letters*, Vol. 24, No. 2, 764–769, 2024.

[43] Wang, K., K. Sun, Q. Ding, L. Zeng, J. Du, Z. Han, L. Huang, and W. Wang, "High-Q resonance engineering in momentum space for highly coherent and rainbow-free thermal emission," *Nano Letters*, Vol. 25, No. 9, 3613–3619, 2025.

[44] Wang, G., E. Maqbool, and Z. Han, "High-Q optical resonances with robustness based on the quasi-guided modes in waveguide moiré gratings," *Optics Express*, Vol. 32, No. 3, 4720–4727, 2024.

[45] Lawrence, M., D. R. Barton III, J. Dixon, J.-H. Song, J. Van de Groep, M. L. Brongersma, and J. A. Dionne, "High quality factor phase gradient metasurfaces," *Nature Nanotechnology*, Vol. 15, 956–961, 2020.

[46] Kim, G., Y. Kim, J. Yun, S.-W. Moon, S. Kim, J. Kim, J. Park, T. Badloe, I. Kim, and J. Rho, "Metasurface-driven full-space structured light for three-dimensional imaging," *Nature Communications*, Vol. 13, 5920, 2022.

[47] Liu, M., Q. Yang, A. A. Rifat, V. Raj, A. Komar, J. Han, M. Rahmani, H. T. Hattori, D. Neshev, D. A. Powell, and I. V. Shadrivov, "Deeply subwavelength metasurface resonators for terahertz wavefront manipulation," *Advanced Optical Materials*, Vol. 7, No. 21, 1900736, 2019.

[48] Tang, W., Q. Zhao, Z. Wang, Y. Gao, J. He, Y. Zhu, S. Wang, H. Yu, R. Peng, and M. Wang, "Realizing high-efficiency third harmonic generation via accidental bound states in the continuum," *Optics Letters*, Vol. 49, No. 5, 1169–1172, 2024.

[49] Hähnel, D., C. Golla, M. Albert, T. Zentgraf, V. Myroshnychenko, J. Förstner, and C. Meier, "A multi-mode super-fano mechanism for enhanced third harmonic generation in silicon metasurfaces," *Light: Science & Applications*, Vol. 12, 97, 2023.

[50] Maqbool, E., A. Rahim, G. Wang, H. Jiang, and Z. Han, "High-Q dielectric metagrating as broadband Raman enhancement substrate enabled by quasi-guided modes," *Optics Express*, Vol. 34, No. 8, 13915, 2026.

[51] Mamoon, I., Q. Liu, M. D. Haque, J. Wang, and S. Wang, "Localized guided-mode resonance-enabled highly angle-insensitive optical filtering," *Optics Letters*, Vol. 51, No. 10, 2972–2975, 2026.